Mo2CTx MXene supported nickel-iron alloy: an efficient and stable heterostructure to boost oxygen evolution reaction

Lola Loupias, Roald Boulé, Cláudia Morais, Vincent Mauchamp, Nadia Guignard, Julie Rousseau, Jérôme Pacaud, Patrick Chartier, Manuel Gaudon, Christophe Coutanceau, et al.

Mo_2CT_x MXene supported nickel-iron alloy: an efficient and stable heterostructure to boost oxygen evolution reaction

Lola Loupias [1], Roald Boulé [1], Cláudia Morais [1], Vincent Mauchamp [2], Nadia Guignard [1], Julie Rousseau [1], Jérôme Pacaud [2], Patrick Chartier [2], Manuel Gaudon [3], Christophe Coutanceau [1], Stéphane Célérier [1,] and Aurélien Habrioux [1,*]*

1. Institut de Chimie des Milieux et Matériaux de Poitiers (IC2MP), Université de Poitiers, CNRS, F-86073 Poitiers, France

2. Institute Pprime, UPR 3346 CNRS, Université de Poitiers, ISAE-ENSMA, BP 30179, 86962 Futuroscope-Chasseneuil Cedex, France

3. CNRS, Univ. Bordeaux, Bordeaux INP, ICMCB, UMR 5026, F-33600 Pessac, France

Abstract. A polyol-assisted solvothermal route is used to synthesize Ni_xFe_y nanoalloys supported on a highly electron conductive 2D transition metal Mo_2CT_x MXene. Structural, morphological and chemical characteristics of the materials are determined using several physicochemical techniques. The MXene support allows not only the formation of a nanostructured metallic Ni_xFe_y nanoalloys, but also favors the interfacial charge transfer for the OER. The Ni_xFe_y@Mo_2CT_x material with a Ni/Fe ratio of 2.66 leads to the outstanding activity for the OER with an amazingly low Tafel slope value of 34 mV dec^{-1} and a current density of 10 $mA.cm^{-2}$ at a potential of only 1.50 V *vs.* RHE. *In situ* Raman experiments show that β-NiOOH formed by oxidation of the nanoalloys under positive scan, likely containing a very small amount of Fe, is the active phase for the OER. This material exhibits also an excellent stability over 168 h in a 5 M KOH electrolyte. TEM-EELS analyses after 100 voltammetric cycles between 0.2 to

1.55 V *vs.* RHE evidence for the first time that the MXene support is not fully oxidized in the first cycle. Also, oxyhydroxide layer formed in the OER potential region at the surface of the Ni_xFe_y nanoparticles can be reversibly reduced.

Keywords. MXene, nickel-iron alloy, molybdenum carbide, oxygen evolution reaction, polyol synthesis route

1. Introduction

The oxygen evolution reaction (OER) plays a key role for the emergence of energy storage and conversion devices such as rechargeable metal-air batteries and electrolyzers required for the implementation of the future energy grid [1-2]. However, the OER involves a complex mechanism with several proton-coupled electron transfer processes and suffers from a sluggish kinetics [3-5]. The use of electrocatalysts can strongly reduce the reaction activation energy and enhance reaction kinetics, prerequisites to allow the future large-scale production of green H_2 and the design of high energy efficiency rechargeable metal-air batteries. The design of efficient catalysts exhibiting a high stability under harsh working conditions encountered in real systems is thus a current major stumbling block.

In alkaline medium, 3d transition metals such as Mn, Ni, Co and Fe are both OER-active materials and thermodynamically stable in the OER potential range. This makes them attractive candidates for the design of low-cost, abundant and noble metal-free catalysts. A wide range of materials combining these elements under various forms have been reported in recent years such as (hydr)oxides [6-8], chalcogenides [9], phosphides [10], nitrides [11], sulfides [12] and borides [13]. Among all possibilities, catalysts combining iron and nickel elements are the most promising ones [14-17].

Several strategies were devised to improve the OER activity of Ni and Fe based electrocatalysts, aiming at exposing more active sites to the electrolyte [18], optimizing the Ni/Fe composition and synthesizing materials with structural defects to regulate the electronic structure [19]. The amazing OER activity of these materials has been ascribed to different phenomena and still remain under debate [20-23]. The understanding of both the dynamic reconstruction and the evolution of the electrode/electrolyte interface induced by variations of the electrode potential must be completed.

These materials are often deposited onto various substrates to improve their dispersion and to avoid aggregation processes under reaction conditions. The strong coupling with conductive materials such as carbon-based substrates [24-28] promotes fast charge transfer at the engineered heterointerface [29] and modulates the local electronic structure of active sites [25, 30]. Nevertheless, the stability of such heterostructures at potentials required for the OER, *i.e.,* higher than 1.23 V *vs.* the reversible hydrogen electrode (RHE), remains questionable [31], the thermodynamic potential of the CO_2/C redox couple being 0.205 V *vs.* RHE.

Two dimensional carbides called MXene have recently attracted much attention as substrates for the deposition of OER active phases[32-35]. MXene sheets, with a general formula of $M_{n+1}X_nT_x$, are obtained from MAX phases (formula : $M_{n+1}AX_n$, with M a transition metal, A generally an element from the 13^{th} or 14^{th} column of the periodic table and X corresponds to carbon and/or nitrogen) by exfoliation of the A element and then delamination [36-40]. The delaminated MXenes present high specific surface areas and electronic conductivity, as well as hydrophilic properties. Terminal groups (T of $M_{n+1}X_nT_x$, generally –O, -OH and/or –F, formed during the exfoliation process) at the surface act as anchoring sites for the active phase, and allow a high chemical versatility to tune the heterointerface interaction and the local electronic

structure of the MXene/active phase [41], making them relevant as supports for active electrocatalysts. However, irreversible oxidation of MXenes occurs at high potential [42, 43], although the oxidation depth remains undetermined. Numerous studies were reported on $Ti_3C_2T_x$ [44-48], $Mo_2TiC_2T_x$ [49] and V_2CT_X [50] substrates for Ni and Fe-based active phases. But, Ti, corresponding to the metallic element most often encountered in MXenes, has recently been included in the list of critical raw materials and has therefore to be avoided in catalyst support formulation. Molybdenum is a non-critical metal and Mo_2CT_x MXenes could be good alternatives to Ti containing MXenes.

Herein, Ni and/or Fe based active phases have been heterogeneously nucleated and grown onto a Mo_2CT_x MXene thanks to a simple polyol-assisted solvothermal method. The use of numerous physicochemical techniques enabled the comprehensive characterization of the morphology, the structure and the composition of the as-synthesized materials. It was first demonstrated that the chemical nature of nickel-iron crystalline phases was influenced by the surface chemistry of the MXene, nanoalloys being successfully synthesized only in the presence of the 2D substrate. The OER activity of NiFe@Mo_2CT_x materials with different Ni/Fe ratios was further determined in alkaline medium. The most efficient heterostructured catalyst led to a particularly high activity: an electrode potential of only 1.5 V *vs.* RHE was required to drive a current density of 10 mA cm^{-2}. *In situ* characterization and characterization of the aged materials (after several potential cycling in the OER potential region) were also performed to get insight on the structural evolution of the composite catalysts.

2. Experimental section

2.1 syntheses of materials

93 The synthesis of Mo_2Ga_2C (MAX-like phase) is performed as described by Benchakar et al.
94 [51]. Gallium is mixed with α-Mo_2C powder (50 μm, 99.5%, Alfa Aesar) in a 1:8 molar ratio.
95 The mixture is crushed in a mortar to obtain a homogeneous paste. The paste is transferred into a
96 vacuum glass tube and thermally treated under argon flow at 850 °C (temperature ramp of 5
97 °C/min) for 7 days. The powder is recovered and treated with hydrochloric acid (35%,
98 TECHNICAL, VWR) overnight under magnetic stirring to remove the excess of gallium. The
99 powder is washed with ultrapure water (MilliQ®, Millipore, 18.2 MΩ at 20 °C), filtered and
100 dried under air. Finally, the powder is sieved in order to select grain sizes lower than 25 μm.
101 The synthesis of Mo_2CT_x is described elsewhere [51]. Briefly, 1 g of the Mo_2Ga_2C powder is
102 put in 20 mL of a 48% HF solution. The mixture is magnetically stirred before being heated at 60
103 °C for 196 h. The suspension is then washed with ultrapure water and centrifuged at 3500 rpm
104 (1575 g) in a rotor F-34-6-38 (Eppendorf centrifuge 5804) several times until the pH value of the
105 supernatant solution is close to 5. The resulting powder is mixed with 5 mL of an aqueous
106 solution of tetrabutylammonium hydroxide (1.5 mol L^{-1} TBAOH aqueous solution, ACROS
107 Organics™) to delaminate the MXene. The mixture is vortexed for 2 min and then ultrasonicated
108 under argon for 30 min to insert TBA^+ ions between MXene sheets. The powder is settled down
109 by centrifugation at 3500 rpm for 2 min, the supernatant solution removed and absolute ethanol
110 (≥ 99.9%, CARLO ERBA) added. The latter procedure is repeated 4 times. Ultrapure water is
111 added and the mixture is centrifuged for 30 min at 2500 rpm (804 g) to form a colloidal
112 suspension of Mo_2CT_x MXene sheets. The suspension is then filtered to recover pure MXene
113 sheets. The retentate is finally dried in a desiccator under atmospheric pressure and the obtained
114 MXene film is placed in a tube and stored in a glove box under argon.

In a tricol, 200 mg of Mo_2CT_x are dispersed in 5 mL of ultrapure water under sonication for 10 min to obtain a colloidal suspension. This mixture is dispersed in 200 mL of anhydrous ethylene glycol (EG, 99.8%, AcroSeal®, ACROS Organics), acting as solvent, before being sonicated for 10 min under argon. Metal precursors (nickel (II) acetate tetrahydrate, ≥ 99.0%, Sigma-Aldrich and/or iron (III) acetylacetonate, ≥ 99.9%, Sigma-Aldrich) are added to the suspension. The solution is magnetically stirred before adding sodium hydroxide (5 g, powder, 97.0%, Sigma-Aldrich). The addition of sodium hydroxide allows the formation of glycolate ions that possess a higher reducing ability than EG [52, 53]. The mixture is then magnetically stirred overnight at room temperature under argon atmosphere and transferred in a Teflon lined autoclave before being heated at 200°C for 3 h under nitrogen flow. The reaction mixture is washed by centrifugation in the presence of ethanol at 9000 rpm for 15 min. The supernatant is removed and the procedure is repeated a second time. A last wash is performed with ultra-pure water. The suspension is filtrated with the addition of 100 mL of ultrapure water. The retentate is placed into a desiccator overnight and stored in a glove box under argon flow. For unsupported materials, the procedure is the same as for supported ones except that the MXene is not added. To determine whether this synthesis route affects the MXene structural properties, the synthesis process was also conducted with MXene without any metallic salts (this material is labelled Mo_2CT_x-ST). The synthesis procedure of the composite is summarized in Scheme S1 of the supplementary information.

The different supported samples are referred to as A/B-NiFe@Mo_2CT_x where A and B are defined as: A = wt.% Ni and B = wt.% Fe. The composition of all the materials investigated in this study is given in Table 1.

Table 1. Nominal weight percent of iron, nickel and Mo_2CT_x in the different investigated samples. The synthesis process was also conducted with MXene without any metallic salts. The sample is labelled Mo_2CT_x-ST.

Label	wt.% Mo_2CT_x	wt.% Ni	wt.% Fe
Fe	0	0	100
Ni	0	100	0
FeNi	0	50	50
33/17-NiFe@Mo_2CT_x	50	33.3	16.7
25/25-NiFe@Mo_2CT_x	50	25	25
17/33-NiFe@Mo_2CT_x	50	16.7	33.3
Mo_2CT_x-ST	100	0	0

2.2 Material characterization

X-Ray diffraction measurements are performed at room temperature over a 2θ angular range, from 3° to 70°, with a step interval of 0.066° and an acquisition time of 420 s per step using an EMPYREAN PANalytical diffractometer in Bragg-Brentano configuration, equipped with a copper anode source ($Cu_{K\alpha1}$ =0.15406 nm). A reduction in analysis time is achieved by using an ultrafast X-ray detector (X'Celerator) based on RTMS (Real Time Multiple Strip) technology. The diffractograms are processed with the HighScorePlus® software.

The morphology of synthesized materials is analysed by scanning electron microscopy (SEM) using a MEB-FEG JSM-7009F microscope (JEOL company) equipped with a field emission gun

and an energy dispersive X-ray spectrometer (EDX) 6/30 from Brücker for the determination of chemical elements in samples. The EDX analyses are performed with the Esprit 2.1 software.

Transmission electron microscopy (TEM) samples are prepared by dispersing the materials in deionized water and dispensing a drop of the suspension on a copper TEM grid covered with a lacy carbon film. TEM analysis including energy filtered selected area electron diffraction (EF-SAED) and electron energy-loss spectroscopy (EELS) are performed using a JEOL 2200-FS microscope operated at 200 kV and equipped with an in-column omega filter. The EELS resolution is around 1.1 eV as determined from the full width at half maximum of the zero-loss peak. The EELS spectra are acquired in image mode using a collection semi-angle of 2.4 mRad. When necessary, spectra are deconvolved from multiple scattering using the Fourier-ratio method.

The size and morphology of nanoparticles supported onto Mo_2CT_x MXene are investigated using a transmission electron microscope (JEOL JEM-2001). Size distributions presented in supporting information are obtained by counting 100 isolated nanoparticles using the ImageJ® free software.

The Mo, Ga, Ni and Fe contents of the different materials are determined by Inductively Coupled Plasma-Optical Emission Spectrometry (ICP-OES) using a PerkinElmer Optima 2000DV instrument.

2.4 Raman spectroscopy measurements

Raman spectroscopy is carried out using a HORIBA Jobin Yvon LabRAM HR800 confocal Raman microscope with a CCD detector. Spectra are acquired at room temperature (RT) using an excitation wavelength of 632.8 nm, supplied by an internal He-Ne laser. The power delivered

is less than 1 mW. An 1800 grooves mm^{-1} grating is used resulting a spectral resolution of 0.5 cm^{-1}. The spectrometer is calibrated with a silicon wafer.

2.5 Electrochemical measurements

Electrochemical measurements are carried out at RT in a home-made three electrode Teflon cell connected to a potentiostat (Biologic SP-300). A reversible hydrogen electrode (RHE) designed for alkaline medium (Hydroflex purchased by Gaskatel) and a glassy carbon (GC) slab are used as reference and counter electrodes, respectively. The working electrode is a 5 mm diameter GC disk (geometric surface area of 0.196 cm^2). A catalytic ink is prepared by dispersing 20 mg of catalytic powder into a solution composed of 500 µL of ultra-pure water (Millipore), 500 µL of isopropanol (Sigma-Aldrich, 99.5%) and 100 µL of Nafion (Sigma Aldrich, 5 wt. % in lower aliphatic alcohols). The ink is homogenized by ultrasonication for 15 min. 3.8 µL of the catalytic ink is deposited onto the glassy carbon disc to reach a catalyst loading of 0.35 mg cm^{-2} and allowed to dry under N_2 (U, Air liquide) atmosphere at room temperature. All measurements are performed in a nitrogen saturated 1 mol L^{-1} KOH electrolyte (≥ 85%, Sigma Aldrich). Cyclic voltammograms and polarization curves are recorded between 0.15 and 1.5 V *vs.* RHE and between 0.8 and 1.8 V *vs.* RHE, respectively. Polarization curves are recorded by applying a rotation rate of 1600 rpm to the rotating disk electrode. IR drop correction of polarization curves is applied. The cell resistance is determined by electrochemical impedance spectroscopy (EIS) in the capacitive region. EIS experiments are also carried out at different electrode potentials in the OER region (potential range from 1.5 to 1.8 V *vs.* RHE). All EIS measurements are recorded with an oscillation amplitude of 10 mV. Impedance spectra are acquired in the 100 kHz to 0.1 Hz region using a Biologic SP-300 potentiostat. Acquired spectra are fitted using the Z-Fit plug-in from EC-lab software (version 11.43).

The same experimental cell is used for stability tests, but the working electrode is a 2 cm^2 geometric surface area nickel foam (Goodfellow, porosity of 95%, purity of 99.5%) impregnated by a catalytic ink containing 40 mg of catalytic powder, 1000 µL of isopropanol, 1000 µL of ultra-pure water and 300 µL of Nafion solution (5wt. % in a mixture of lower aliphatic alcohols). Stability tests are performed in N_2-purged 1 M and 5 M KOH electrolytes. Chronopotentiometric measurements are performed by applying a constant current of 20 mA (current density of 10 mA cm^{-2}_{geo}).

In situ Raman spectroscopy measurements are performed in a home-made electrochemical cell equipped with a reference hydrogen electrode (purchased by Gaskatel company), a counter electrode (glassy carbon slab) and a working electrode (glassy carbon disk with a diameter of 5 mm). The working electrode is prepared in the same way as for the cyclic voltammetry measurements (see above). Before recording Raman spectra, the catalyst is cycled 100 times between 0.8 and 1.45 V *vs.* RHE to stabilize the catalytic surface. To get a better signal, Raman spectra are recorded without any window as described in reference [54]. A long-distance microscope objective (Olympus 50x) is used. A 514 nm exciting wavelength is employed and the power of the laser source is set at 4 mW. Spectra are acquired using a diffraction grating with 1800 grooves mm^{-1} and a confocal hole of 200 µm. The Labspec 5 software is used for the acquisition of spectra as well as for the analysis of experimental data.

3. Results and discussion

3.1 Characterization of materials

The Mo_2CT_x MXene support has been synthesized by exfoliation of the Mo_2Ga_2C MAX like-phase followed by delamination in TBAOH and then, the $Ni_xFe_y@Mo_2CT_x$ materials by a

polyol-assisted solvothermal synthesis route. The polyol-assisted solvothermal procedure has also been applied to the MXene alone (referred to as Mo_2CT_x-ST) to further investigate possible induced structural changes. At last, unsupported Ni, Fe and NiFe catalysts have been synthesized to compare their structure with those of the MXene-supported ones. All experimental X-ray diffraction patterns are plotted in Figure 1.

The XRD pattern of the Mo_2Ga_2C powder is given in Figure 1a. A phase purity of 97.3(2) % is estimated from the Rietveld refinement performed on the XRD pattern in the 5-120° angular range (data not shown), the impurities corresponding to 0.6(2) % of α-Mo_2C and 2.1(1) % of Mo_2GaC. For the Mo_2CT_x and Mo_2CT_x–ST materials (Figure 1a), the absence of the sharp diffraction peak at 9.9 ° evidences the formation of a pure MXene phase validating the selected procedure to separate the unreacted Mo_2Ga_2C MAX-like phase from the MXene during the polyol-assisted solvothermal process. This fact is further confirmed by ICP-OES analysis of the MXene powder that reveals a very low amount of Ga (0.03 Ga atom for 2 Mo atoms). For the Mo_2CT_x MXene sample, the c parameter value of the hexagonal lattice calculated from the position of the broad (002) diffraction peak is about 22.5 Å, in agreement with already reported values [51]. For the Mo_2CT_x-ST sample, the value of the c parameter is ca. 21.2 Å, *i.e.*, very close to the value obtained for the pristine Mo_2CT_x (22.5 Å). As described in a previous work [55], the interstratification phenomenon often at stake with MXene leads to noticeable variation on the c parameter due to hydration heterogeneities in-between the sheets. Herein, no significant modification of the interlayer spacing value was observed and consequently it can be stated that the polyol-assisted solvothermal treatment has little impact on the MXene structure.

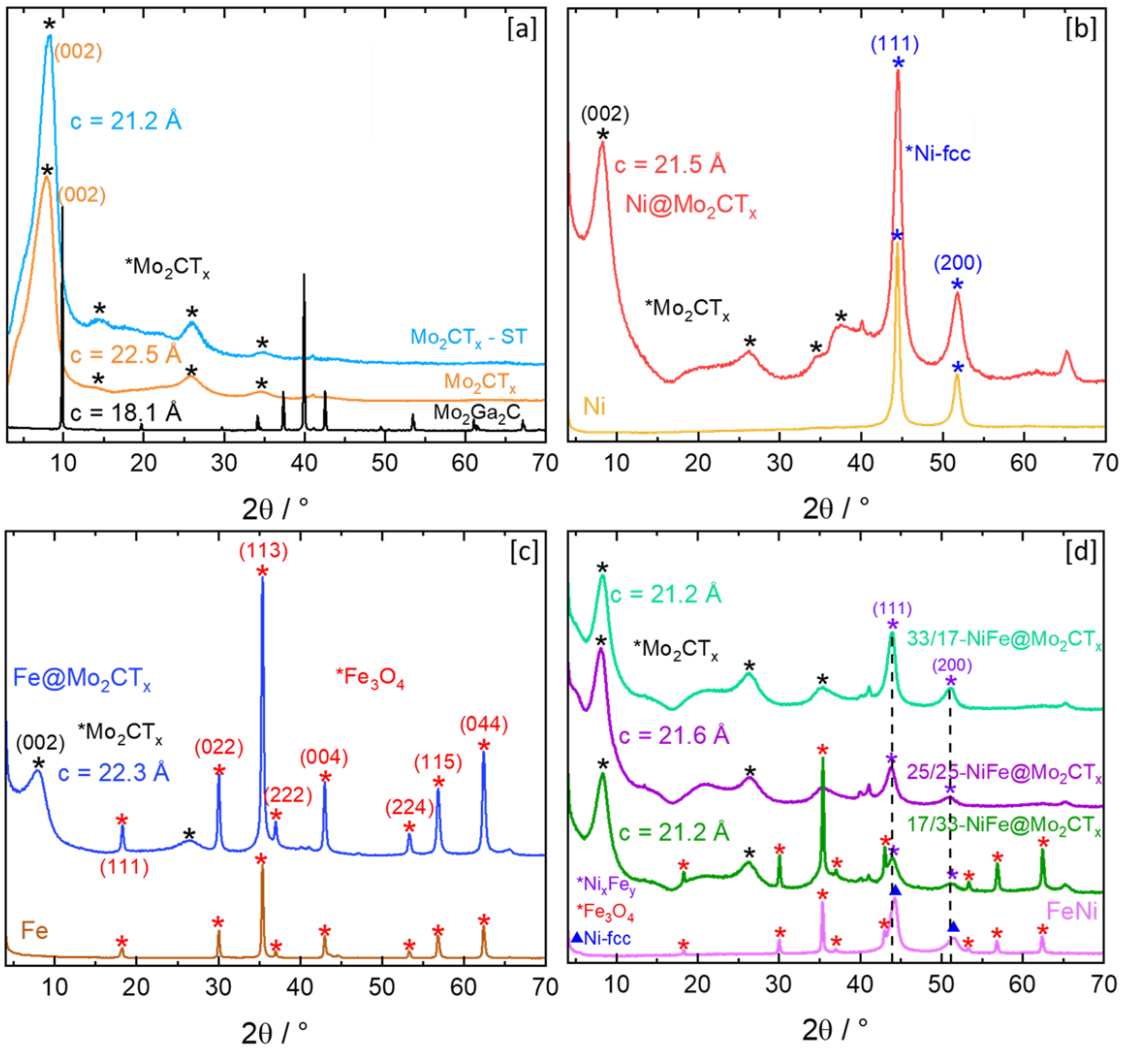

Figure 1. X-ray diffraction patterns recorded for: (a) Mo_2Ga_2C, Mo_2CT_x and Mo_2CT_x-ST; (b) Ni and Ni@Mo_2CT_x (c) Fe and Fe@Mo_2CT_x; (d) 33/17-NiFe@Mo_2CT_x, 25/25-NiFe@Mo_2CT_x, 17/33-NiFe@Mo_2CT_x and FeNi materials.

For MXene-supported Ni_xFe_y materials (Figures 1b to 1d), the c parameter values of the Mo_2CT_x support lie between 21.5 and 22.3 Å, confirming again that non-significant changes in the chemical nature of molecules and ions intercalated in the interlayer spacing occur during the synthesis process. Moreover, no diffraction peak corresponding to molybdenum oxides could be identified, showing that the MXene is not oxidized, which is not so surprising since the synthesis is performed in a reducing environment (ethylene glycol). This observation is of upmost

importance since the preservation of the MXene structural properties (and thus of its electronic conductivity) is mandatory to obtain efficient heterostructured electrocatalysts. This point is often neglected in literature where for numerous composite catalysts recently reported, the MXene support was strongly oxidized during the synthesis [56, 57].

Regarding the XRD patterns of single metal (Fe or Ni) unsupported samples, features corresponding to Ni-fcc phase (01-089-7128 JCPDS file) and Fe_3O_4 spinel phase (98-008-2453 JCPDS file) are observed. The diffraction pattern of the unsupported FeNi material (Fig. 1d) is only a linear combination of those recorded for unsupported Ni and Fe materials (Figure 1b and 1c), *i.e.,* a mixture of Ni-fcc and Fe_3O_4 phases; no alloyed phase of Fe and Ni elements could be identified. These phases are also observed in the Ni@Mo_2CT_x and Fe@Mo_2CT_x samples, respectively, in addition to that of the MXene. Interestingly, the diffraction patterns of the 25/25-NiFe@Mo_2CT_x and 33/17-NiFe@Mo_2CT_x materials (Figure 1d) do not show any signal of the Fe_3O_4 phase but a shift of the 111 and 200 diffraction peaks of fcc-Ni phase towards lower angles testifies the presence of a new single face centered cubic Ni_xFe_y nanoalloy phase in agreement with the incorporation of iron in the Ni-fcc phase (metal radii are 126 pm and 124 pm for Fe and Ni, respectively). The Ni-Fe phase diagram predicts indeed the existence of a large fcc solid solution above 30 mol% of nickel [58]. For the 17/33-NiFe@Mo_2CT_x sample (Figure 1d), the signature of Fe_3O_4 phase can again be observed. For Fe-rich materials, the reducing conditions are not strong enough to force the iron element to participate to the nanoalloy germination-growth. As a conclusion, the transition from homogeneous to heterogeneous germination when Mo_2CT_x is introduced may favor the stabilization and thus the growth of Ni_xFe_y nanoalloys, a clear advantage to get a highly efficient electrocatalyst as discussed latter in this manuscript.

The crystallite sizes of Fe_3O_4 and Ni catalysts are estimated using Scherrer's law [59]. The full width at half maximum was determined by assuming Lorentzian line profiles and the instrumental width determined using a LaB_6 standard powder is subtracted. The crystallite sizes of unsupported Ni and Fe_3O_4 materials are ca. 27 nm and ca. 45 nm, respectively. The crystallite size of Ni and Fe_3O_4 catalysts in Ni@Mo_2CT_x and Fe@Mo_2CT_x composites are ca. 13 and ca. 35 nm, respectively, indicating a lower crystallinity than for the unsupported ones.

Particle size distributions of Fe_3O_4 and Ni catalysts was established by measuring 100 particles from high magnification TEM images (Figure S1). For unsupported Ni and Fe samples the mean particle sizes are ca. 123 and ca. 57 nm, respectively, whereas for Ni@Mo_2CT_x and Fe@Mo_2CT_x samples they are ca. 17 and ca. 40 nm, respectively. The nucleation process is energetically favored in the presence of the MXene support (heterogeneous nucleation) allowing multiplying the number of nucleation sites and enabling the probable formation of smaller particles than in the case of homogeneous nucleation leading to unsupported particles.

The crystallite sizes of Ni_xFe_y catalysts in 25/25-NiFe@Mo_2CT_x, 33/17-NiFe@Mo_2CT_x and 17/33-NiFe@Mo_2CT_x samples are ca. 12, 12 and 16 nm, respectively. Because the 17/33-NiFe@Mo_2CT_x sample contains both Ni_xFe_y and Fe_3O_4 phases, it is not possible to discriminate the size of Fe_3O_4 and Ni_xFe_y particles from TEM images. The mean particle sizes are thus only determined for the 25/25-NiFe@Mo_2CT_x and 33/17-NiFe@Mo_2CT_x samples (Figure S1). For both samples, mean particle sizes are much greater than crystallite sizes (for example, mean particle size of 60 nm and crystallite size of 12 nm for the 33/17-NiFe@Mo_2CT_x samples). This probably results from the formation of polycrystalline particles. Anyway, the very small crystallite sizes calculated for both composites tend to confirm that the presence of the MXene

support favors the nucleation step at the expense of the growth step, leading to the formation of Ni_xFe_y nanoalloys rather than to phase segregations.

SEM experiments are performed to investigate the morphology of the different materials. Scanning electron micrographs of Mo_2Ga_2C, Mo_2CT_x MXene and 25/25-NiFe@Mo_2CT_x are shown in Figure S2. Mo_2Ga_2C exhibits a typical platelet morphology with crystals that have a lateral size ranging from 1 to 10 microns (Figures S2a and S2b) [60, 61] while the Mo_2CT_x sample (Figures S2c and S2d) exhibits a typical film-like morphology. Sheets formed by Mo_2CT_x multi-layers with intersheet gaps (Figures S2d) display a relatively smooth surface (Figures S2c), and the different multi-layers are more or less wrapped owing to the restacking of delaminated MXene sheets after filtration [60-63]. After the polyol-assisted solvothermal synthesis of composite materials, the sheets appear coated by aggregated Ni_xFe_y nanoparticles both on the top surface and on the edge of Mo_2CT_x layers constituting the sheets (Figures 2e and 2f for the 25/25-NiFe@Mo_2CT_x composite). Large scale elemental mapping analyses were performed on 25/25-NiFe@Mo_2CT_x, 33/17-NiFe@Mo_2CT_x and 17/33-NiFe@Mo_2CT_x samples (Figure S3). Spectral regions associated to the combination of all elements, Ni, Fe and Mo elements were specifically analyzed. Regarding the combination of elements (Figure S3b), it is clear that 17/33-NiFe@Mo_2CT_x contains two different kinds of particles: those only composed of Fe, associated to Fe_3O_4 phase and those composed of a combination of Ni and Fe elements, associated to Ni_xFe_y nanoalloy. Only the presence of alloyed particles can be observed with other samples in agreement with XRD characterizations.

The chemical compositions of the different materials have been determined by ICP-OES. Mo, Ni and Fe elements were quantified and results are given in Table 2.

Table 2: Chemical composition of supported and unsupported materials determined by ICP-OES. Nominal Ni/Fe molar ratio corresponds to the ratio expected from the introduced amounts of metal salts.

Sample	wt. %				Nominal Ni/Fe molar ratio	Experimental Ni/Fe molar ratio
	Mo	Ni	Fe	$Mo_2C(OH)_2$		
Ni	-	91.6	-	-	-	-
FeNi	-	55.4	29.5	-	0.95	1.79
Fe	-	-	78.6	-	-	-
Ni@Mo_2CT_x	21.4	59.2	-	26.5	-	-
Fe@Mo_2CT_x	15.1	-	52.3	18.7	-	-
33/17-NiFe@Mo_2CT_x	29.7	38.0	9.0	36.8	1.90	4.02
25/25-NiFe@Mo_2CT_x	33.8	29.9	10.7	41.9	0.95	2.66
17/33-NiFe@Mo_2CT_x	21.3	20.4	32.3	26.4	0.47	0.60
Mo_2CT_x-ST	63.6	-	-	78.8	-	-

The targeted loadings for MXene in composites materials (50 wt.%) are calculated assuming the chemical formula $Mo_2C(OH)_2$ with a molar mass of 237.89 g mol^{-1}. This chemical formula does not consider water and cations (TBA^+) potentially inserted in the multi-layers of MXene sheets, explaining that the calculated MXene loadings remain always lower than the targeted ones. For 17/33-NiFe@Mo_2CT_x and Fe@Mo_2CT_x materials, the oxygen content drastically increases due to the presence of the Fe_3O_4 phase as evidenced by XRD measurements (Figure 1), leading to a bias in the quantification. In addition, some molecules from the solvents used for the polyol-assisted solvothermal synthesis and the washing steps probably remain trapped between the MXene sheets and/or in the interstices of Ni_xFe_y nanoparticle agglomerates, which for instance could explain the value of 92 wt.% for the unsupported Ni sample instead of 100 wt.%. For materials with bimetallic Fe-Ni catalysts, the experimental Ni/Fe ratio is systematically and in a reproductible manner (Ni/Fe ratio similar from one synthesis to another one) higher than the

expected one suggesting a systematic loss of iron during the synthesis procedure. However, the reproducibility ensures the control of the final ratio in the materials.

Raman spectroscopy is used to investigate the oxidation state of the MXene and the chemical nature of terminal groups. Raman spectra are acquired in the 85 – 830 cm^{-1} spectral range for the Mo_2Ga_2C, Mo_2CT_x, Mo_2CT_x-ST and 25/25-NiFe@Mo_2CT_x samples (Figure S4). No peaks corresponding to molybdenum oxide is identified, confirming that the MXene surface is not oxidized during the nucleation and growth of Ni_xFe particles. However, the polyol-assisted solvothermal procedure affects noticeably the nature of the terminal groups of the MXene by replacing fluorine with oxygenated groups. Details on the Raman study and assignment of peaks can be found in the 'Raman spectroscopy' section of the supplementary information.

The microstructure and chemistry of the 25/25-NiFe@Mo_2CT_x material (the most efficient material for the OER, see further) is investigated by TEM/EF-SAED (Figures 2a to 2d) and EELS (Figure 2e). Figure 2a displays a dense network of nanoparticles, Figures 2b and 2c focus on several particles to observe their general shape and size. Dark lines (highlighted by arrows) are ascribed to small MXene sheets, in agreement with the detection of the C-K edge by EELS (Figure 2e), although the signal is very low probably due to the small amount of Mo_2CT_x sheets in the irradiated area delimited by the red circle (a defocused electron beam is used to minimize beam damage). The Feret's diameter of Ni_xFe_y nanoparticles is estimated to ca. 20 nm, in agreement with XRD and TEM characterizations. The typical EF-SAED pattern in Figure 3d is correctly indexed considering a Ni_xFe_y-fcc structure, confirming the XRD results. The analysis of Fe-$L_{2,3}$ and Ni-$L_{2,3}$ edges from EELS measurements (shown in Figure S9 for comparison with characterization of aged materials) leads to particle composition between $Ni_{2.9}Fe$ and $Ni_{3.7}Fe$, in agreement with ICP measurements ($Ni_{2.66}Fe$) considering the uncertainty on the quantifications.

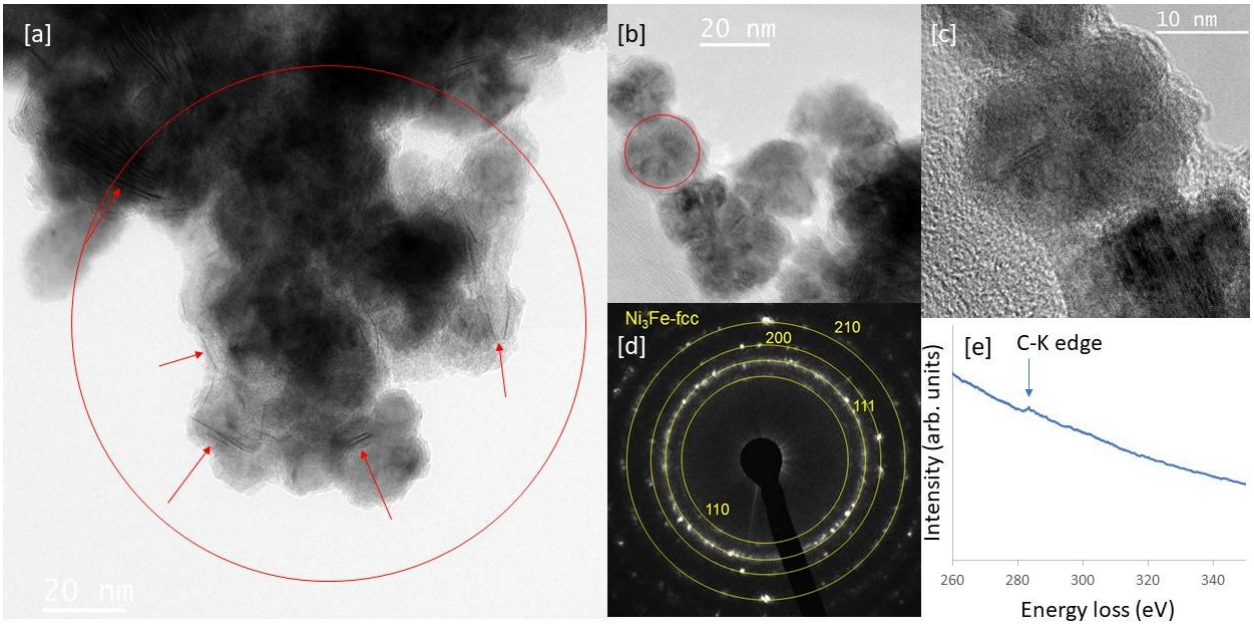

Figure 2: (a) to (c) micrographs recorded on different areas of a TEM grid prepared from the 25/25-NiFe@Mo_2CT_x sample. In (a) arrows identify elongated contrasts, (c) gives a magnification of the nanoparticle highlighted in red in (b), (d) typical energy-filtered selected area diffraction pattern showing that nanoparticles essentially have a fcc-Ni_xFe structure and (e) C-K edge recorded using EELS on the area identified by a red circle in (a).

Chemical analysis performed by EELS point out the presence of a non-negligible amount of oxygen in the sample (Figure 3a). The O-K edge exhibits a well-defined fine structure with a main peak B and different signatures of lower intensity labelled A, C and D, very similar to that reported on $NiFe_2O_4$ [64, 65]. Energy-Filtered TEM (EFTEM) at the O-K edge using the jump ratio method is used to map the oxygen distribution in nanoparticles (Figures 3b). Clearer areas evidence oxygen enrichment around the particles. Intensity profiles extracted through two particles and integrated over 30 pixels (Figures 3c and 3d) clearly show oxygen enrichment on the outer edge of the nanoparticles. This result is not surprising since metallic alloys such as Ni_xFe_y are subject to surface oxidation when exposed to air. The low thickness of the shell and

the oxygen concentration gradient from bulk to surface of the nanoparticles indicate that this oxide is rather amorphous, and therefore not detectable by XRD. Moreover, the Raman spectrum of the material (Figure S4) does not exhibit any visible vibrational feature corresponding to the nearly spinel-like phase shell surrounding Ni_xFe_y nanoparticles observed by TEM-EELS technique, likely owing to the lack of long-range ordering and/or the low amount of matter composing this shell.

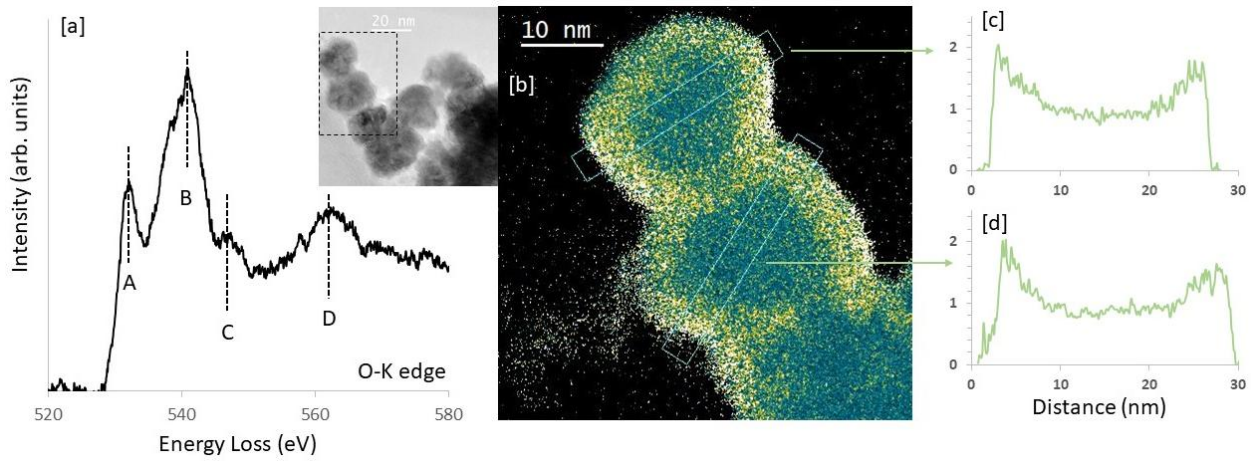

Figure 3. (a) Typical O-K edge recorded in various areas of the 25/25-NiFe@Mo_2CT_x sample. (b) EFTEM micrograph at the O-K edge recorded using the jump ratio method (white areas evidence oxygen enrichment on the outer part of the nanoparticles) and (c) corresponding intensity profiles extracted along the two directions evidenced by the rectangles (intensities were integrated over 30 pixels).

3.2 Electrochemical measurements

The electrochemical behavior of the different composite materials was investigated and compared to that of Mo_2CT_x-ST. Figure 4a presents the first voltammetric cycles recorded between 0.1 and 1.55 V *vs.* RHE in a nitrogen-purged 1 M KOH supporting electrolyte on the different materials.

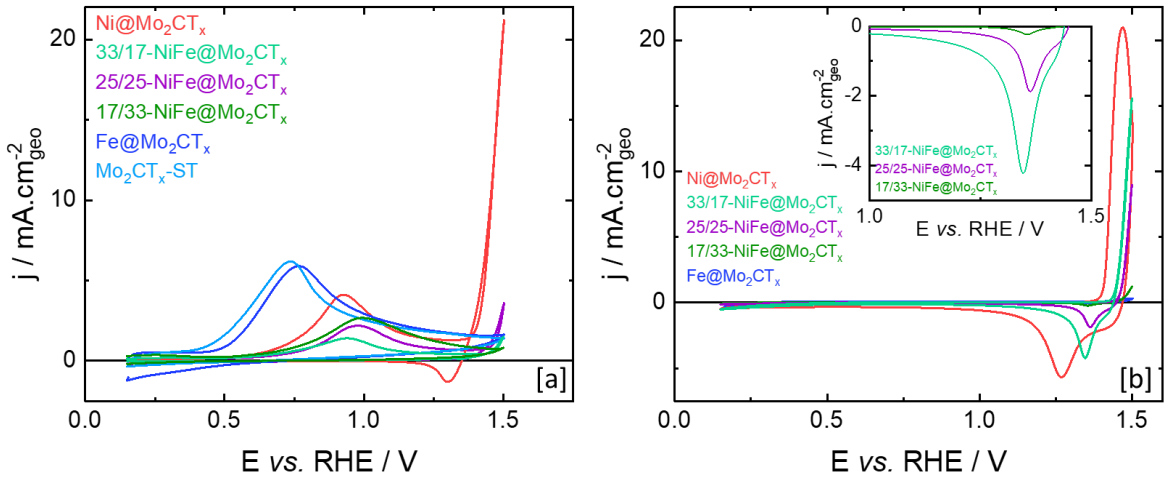

Figure 4. (a) First cyclic voltammogram recorded with the different composite materials ($Ni@Mo_2CT_x$, $Fe@Mo_2CT_x$, $17/33\text{-}NiFe@Mo_2CT_x$, $25/25\text{-}NiFe@Mo_2CT_x$ and $33/17\text{-}NiFe@Mo_2CT_x$) and Mo_2CT_x-ST MXene. (b) 100th voltammetric cycle recorded with $Fe@Mo_2CT_x$, $17/33\text{-}NiFe@Mo_2CT_x$, $25/25\text{-}NiFe@Mo_2CT_x$ and $33/17\text{-}NiFe@Mo_2CT_x$ and $Ni@Mo_2CT_x$. All voltammograms are recorded in a nitrogen saturated KOH 1 M electrolyte. The scan rate is set at 50 mV s^{-1}.

In all cases, an irreversible oxidation peak is rising between 0.5 and 1.0 V *vs.* RHE in the positive going scan, which is due to the oxidation of the material surface. Because this oxidation peak also appears for Mo_2CT_x alone, it is ascribed to the oxidation of the MXene according, by analogy with the recently reported electrochemical behavior of $Ti_3C_2T_x$ [42, 43], to the following equation:

$$Mo_2CT_x + 6HO^- \rightarrow 2MoO_2 + CO + 3H_2O + xT^- + (6\text{-}x)e^- \quad (1)$$

Electrochemical signatures of Mo_2CT_x and Mo_2CT_x-ST are quite similar (Figure S5). The presence of the irreversible oxidation peak indicates that MXene surface is not oxidized in course of the polyol-assisted solvothermal synthesis in accordance with previous characterizations, and thus redox properties of Mo atoms are kept. The coulometry in the irreversible oxidation peak of Mo_2CT_x-ST seems to be higher than that of Mo_2CT_x. It is likely that the polyol-assisted solvothermal treatment favors delamination of MXene sheets, leading to increase the surface of

MXene exposed to the electrolyte. In a catalytic point of view, an increase of the support specific surface area is very positive for a higher dispersion of the active phase.

The position of the irreversible oxidation peak of Fe@Mo_2CT_x, Ni@Mo_2CT_x 33/17-NiFe@Mo_2CT_x, 25/25-NiFe@Mo_2CT_x and 17/33-NiFe@Mo_2CT_x materials is shifted towards higher potentials: 0.77, 0.93, 0.93, 0.98 and 0.99 V *vs.* RHE, respectively, against 0.73 V *vs.* RHE for Mo_2CT_x-ST. The presence of the active phase stabilizes the MXene surface and delays its oxidation [66, 67], possibly due to changes in electron density of state of the surface Mo atoms. Ni@Mo_2CT_x produces a large oxidation wave at potentials higher than 1.4 V *vs.* RHE in the positive potential scan and a reduction peak at 1.3 V *vs.* RHE in the negative scan, corresponding to Ni^{2+}/Ni^{3+} redox transition.

The irreversible MXene oxidation signal doesn't appear in the second voltammetric cycle (Figure S6), indicating that the surface of the MXene exposed to the electrolyte is totally passivated in the first cycle. However, the Ni_xFe_y active phases need several voltammetric cycles to give stable electrochemical signatures (data not shown). Figure 4b presents the 100th voltammetric cycle recorded on each material. No signal of iron redox transition is observed on the voltammogram of Fe@Mo_2CT_x, in agreement with literature [68-70]. On contrary, Ni@Mo_2CT_x leads to well-defined redox signals centered at ca. 1.46 V (oxidation) and 1.28 V (reduction) *vs.* RHE corresponding to the $Ni(OH)_2$/NiOOH transition. For nickel-iron based composites, the Ni^{2+}/Ni^{3+}oxidation wave is shifted towards higher potentials and overlaps with the OER current, and the reduction peak appears at ca. 1.36, 1.37 V and 1.34 V *vs.* RHE for 17/33-NiFe@Mo_2CT_x, 25/25-NiFe@Mo_2CT_x and 33/17-NiFe@Mo_2CT_x, respectively, i.e., at potential 60 to 90 mV higher than that for Ni@Mo_2CT_x. The stabilization of Ni^{2+} state, thanks to

the presence of iron [22], induces an increase of the oxidizing power of nickel species formed at potentials of the OER, and thus the enhancement of the OER activity (see below).

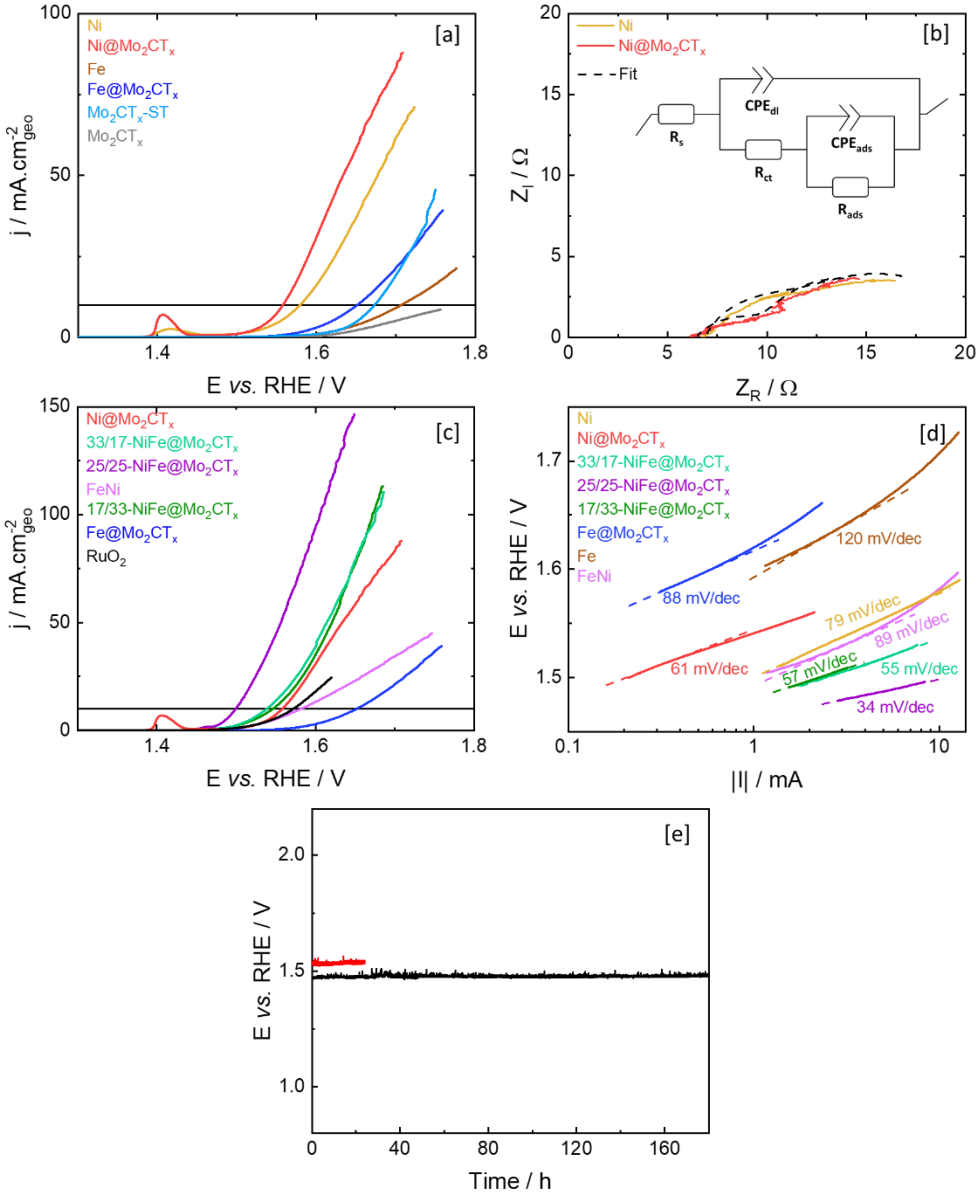

Figure 5. (a) Polarization curves recorded with different materials in nitrogen-purged 1 M KOH electrolyte. (b) Impedance spectra recorded at 1.60 V *vs.* RHE for Ni and Ni@Mo_2CT_x samples and equivalent circuit model used to fit experimental electrochemical impedance spectra. (c) Polarization curves recorded on supported composites and FeNi sample in nitrogen-purged 1 M KOH. (d) Tafel plots determined from polarization curves presented in (a) and (c). (e) Chronopotentiometry performed on the 25/25-NiFe@Mo_2CT_x material in nitrogen-purged 1 M KOH (red) and 5 M KOH (black) electrolytes, i = 20 mA (current density of 10 mA cm^{-2}_{geo}).

444 The OER activity of the materials is investigated in 1 M KOH aqueous medium by recording
445 polarization curves in the 1.2 V to 1.8 V *vs.* RHE potential range (Figure 5a). The OER activity
446 of Mo_2CT_x-ST appears higher than that for Mo_2CT_x sample owing to the larger electrochemical
447 surface area of Mo_2CT_x-ST MXene (higher coulometry for Mo oxidation – Figure S5) than that
448 of the Mo_2CT_x sample (Figure S5). Ni@Mo_2CT_x and Fe@Mo_2CT_x composites are more active
449 than the corresponding unsupported Ni and Fe catalysts, although their Ni and Fe contents are
450 drastically lower (Table 2). A current density of 10 mA cm^{-2}_{geo} is reached at 1.56 V and 1.65 V
451 *vs.* RHE for Ni@Mo_2CT_x and Fe@Mo_2CT_x, respectively, against 1.58 V and 1.71 V *vs.* RHE for
452 unsupported Ni and Fe catalysts, respectively. The promotional effect of the MXene support can
453 originate from the induced lower Ni and Fe mean particle sizes than in the case of non-supported
454 Ni and Fe catalysts, leading to higher electroactive surface area (ESCA) of supported materials,
455 and/or from a strong MXene/active phase interaction promoting charge transfer and increasing
456 OER activity.
457 The determination of the ESCA of such materials is not always possible ("Discussion on the
458 determination of ECSA value" section in supplementary information). The most reliable
459 technique consists to estimate the Ni ECSA in samples through the coulometry associated with
460 the one electron reduction of NiOOH into $Ni(OH)_2$. But this method cannot be used for Fe-based
461 samples (no coulometry due to Fe redox) or NiFe-based samples since redox properties of Ni are
462 altered (stabilization of Ni^{2+}) in the presence of iron (Figure 5). Therefore, ESCAs have been
463 determined only for non-supported Ni and Ni@Mo_2CT_x materials. From voltammograms in
464 Figure S8a, and considering a charge of 257 μC cm^{-2} for the Ni^{2+}/Ni^{3+} redox process occurring
465 on a flat smooth nickel electrode [71, 73], ECSAs were calculated and normalized polarization
466 curves drawn (Figure S8b). Both materials lead to similar surface activity, meaning that size

effect cannot be neglected. The charge transfer resistance for the OER is estimated from electrochemical impedance spectra at 1.6 V *vs.* RHE, after fitting of the data based on the Armstrong-Henderson equivalent circuit (Figure 5b) [74]. R_s corresponds to the cell resistance (resulting from electrical connections, electrolyte, and catalytic deposit) and the CPE_{dl} constant phase element models the double-layer capacitance taking into account the surface roughness and non-uniform distribution of active sites [75]. R_{ct} and R_{ads} represent the charge transfer resistance and the mass transfer resistance associated to adsorbed intermediates at the electrode surface, respectively. The sum of R_{ct} and R_{ads} corresponds to the total faradaic resistance (R_{far}), which is the descriptor of the kinetics of the OER [76]. CPE_{ads} mimics the charge for the reversible adsorption of OER intermediates [74]. Values of R_s, R_{ct}, R_{ads} and R_{far} calculated from the best fit are reported in Table 3.

Table 3: Values of R_s, R_{ct}, R_{ads} and R_{far} parameters obtained by simulating the electrochemical impedance spectroscopy data.

Sample	R_s (Ω)	R_{ct} (Ω)	R_{ads} (Ω)	R_{far} (Ω)
Ni	6.9	6.5	7.6	14.1
Ni@Mo_2CT_x	6.5	4.5	7.4	11.9

R_s value remains constant (as expected), as well as R_{ads}, whereas R_{far} value is lower for the Ni@Mo_2CT_x material than that for the non-supported Ni catalyst mainly due to the decrease of the R_{ct} value. This is an important result that suggests that the passivation (oxidation) of the MXene does not occur at the interface Ni/MXene support, and that rapid charge transfer between the Ni active phase and the support is not affected. Another important conclusion is that both effect, size and charge transfer, are involved in the activity enhancement for the OER of the

488 Ni@Mo_2CT_x material. We can reasonably assume that this is also the case for NiFe@Mo_2CT_x
489 materials.

490 The OER activity of nanocomposites containing both Ni and Fe metals is higher than for
491 Fe@Mo_2CT_x, Ni@Mo_2CT_x catalysts and unsupported NiFe material (Figure 5c). The activity of
492 Ni/Fe mixed composites depends on the iron content with a maximum for the 25/25-
493 NiFe@Mo_2CT_x material containing fcc-$Ni_{2.66}Fe$ particles (Table 2). This material allows
494 reaching 10 mA cm^{-2} at a potential of only 1.50 V *vs.* RHE. The positive impact of Fe on Ni
495 active sites in nanoalloys is known [14, 15, 22, 77-80], but the 25/25-NiFe@Mo_2CT_x material is
496 one of the most efficient MXene-based catalysts ever reported to date (Table S1). Catalysts
497 deposited onto 3D electrodes (Ni foam) can outperform the 25/25-NiFe@Mo_2CT_x material, but a
498 direct comparison of the geometric current density is not fair because the porous structure of Ni
499 foam increase dramatically the specific surface area whereas only projected surface areas is
500 considered to normalize polarization curves. Furthermore, the electrochemical performances
501 obtained herein with 25/25-NiFe@Mo_2CT_x catalyst are better than those obtained with a
502 reference catalyst, a commercial RuO_2 (E_{j10} = 1.57 V *vs* RHE) (Figure 5).

503 The OER activities of 33/17-NiFe@Mo_2CT_x (containing only Ni_xFe_y nanoparticles) and 17/33-
504 NiFe@Mo_2CT_x (containing a mixture of Ni_xFe_y and Fe_3O_4 particles) are quite similar, but lower
505 than that of the 25/25-NiFe@Mo_2CT_x material: current density of 10 mA cm^{-2} at 1.53 V, 1.54 V
506 and 1.37 V *vs.* RHE, respectively. The Ni_xFe_y nanoalloy in the 33/17-NiFe@Mo_2CT_x material
507 contains less Fe than the 25/25-NiFe@Mo_2CT_x one (Table 2, last column), so that the Ni
508 oxidizing power is decreased (Figure 4b) and hence the OER activity; moreover, larger Ni_xFe
509 particle size (Figure S1) decreases the ESCA and therefore activity. For the 17/33-
510 NiFe@Mo_2CT_x material, the presence of a large amount of inactive Fe_3O_4 phase observed by

511 XRD (Figure 1) means that the active surface area of Ni_xFe_y is lowered, and thus the OER
512 activity. In our case the optimum Ni/Fe ratio is close to 2.66.

513 The Tafel slopes are determined from steady state current density recorded versus applied
514 electrode potential in the low overpotential region (Figure 5d). Tafel slope values are
515 significantly lower for the Ni@Mo_2CT_x and Fe@Mo_2CT_x materials compared to their respective
516 non-supported catalysts, *i.e.*, an increase in the rate of the determining step owing to an improved
517 charge transfer. The higher activity of Ni and Ni@Mo_2CT_x materials observed in Figure 5a is
518 confirmed by the Tafel slope values of 79 and 61 mV dec^{-1}, respectively (against 88 and 120 mV
519 dec^{-1} for Fe and Fe@Mo_2CT_x materials, respectively), suggesting the second chemical reaction
520 process as rate determining step [16]. The Tafel slope value of 57 mV dec^{-1} for the 17/33-
521 NiFe@Mo_2CT_x materials decreases down to 34 mV dec^{-1} for the 25/25-NiFe@Mo_2CT_x one,
522 showing that the rate determining step shifts from the second chemical step to the recombination
523 of adsorbed –O at the catalytic surface [81]. The surface structure and the arrangement of Ni and
524 Fe atoms in the 25/25-NiFe@Mo_2CT_x material favor the formation of O-O bond (last step of the
525 OER mechanism). The Tafel slope value obtained with the 25/25-NiFe@Mo_2CT_x material is the
526 lowest ever reported for catalysts consisting of a Ni- and Fe-based active phase supported on a
527 MXene (Table S1). Although E_{j10} values are rather similar for all materials (Table S1), the
528 25/25-NiFe@Mo_2CT_x sample will possibly allow driving a current density of 1 A cm^{-2}_{geo} (the
529 minimum targeted current density in electrolysis cells) at lower electrode potentials, which is
530 crucial for the large-scale commercialization of alkaline water electrolyzers.

531 The long-term stability of the 25/25-NiFe@Mo_2CT_x material is investigated in 1 M and 5 M
532 KOH aqueous electrolyte at RT by chronopotentiometry at the constant current density of 10 mA
533 cm^{-2}_{geo} (Figure 5e). The electrode potential remains at a constant value of 1.48 V *vs.* RHE for 7

days in a 5 M KOH electrolyte, showing the high stability of the synthesized material and making it a promising catalyst for the implementation of emerging solid electrolyte alkaline electrolyzers. To investigate the nature of the active sites formed at OER potentials, *in situ* Raman spectra were recorded at different electrode potentials (1.30, 1.35, 1.40, 1.45, 1.50, 1.55 V *vs.* RHE) in the 300-1000 cm^{-1} spectral window (Figure 6) on the 25/25-NiFe@Mo_2CT_x sample. The spectrum recorded at 1.3 V *vs.* RHE (potential higher than the irreversible oxidation potential of Mo_2CT_x) doesn't show any feature corresponding to either molybdenum oxide or to terminal groups grafted on the Mo_2CT_x surface. Three Raman bands appear at *ca.* 487, 573 and 690 cm^{-1} for electrode potential between 1.35 V and 1.45 V *vs.* RHE, which can be ascribed to the doubly degenerated T_{2g} and A_{1g} modes of the spinel phase [54]. For higher potentials, i.e. in the OER potential region, the vibrational features of the spinel phase disappear while two new bands are observed at ca. 475 cm^{-1} and 557 cm^{-1}, which can be ascribed to M-O vibrations of Ni oxyhydroxyde probably containing also Fe atoms. On the basis of the band positions, it is difficult to discriminate the formation of either γ-Ni(Fe)OOH or β-Ni(Fe)OOH [79]. Nevertheless taking into account the intensity ratio of these two bands [82], β-Ni(Fe)OOH is probably formed, implying that β-Ni(Fe)OOH would be the OER active phase.

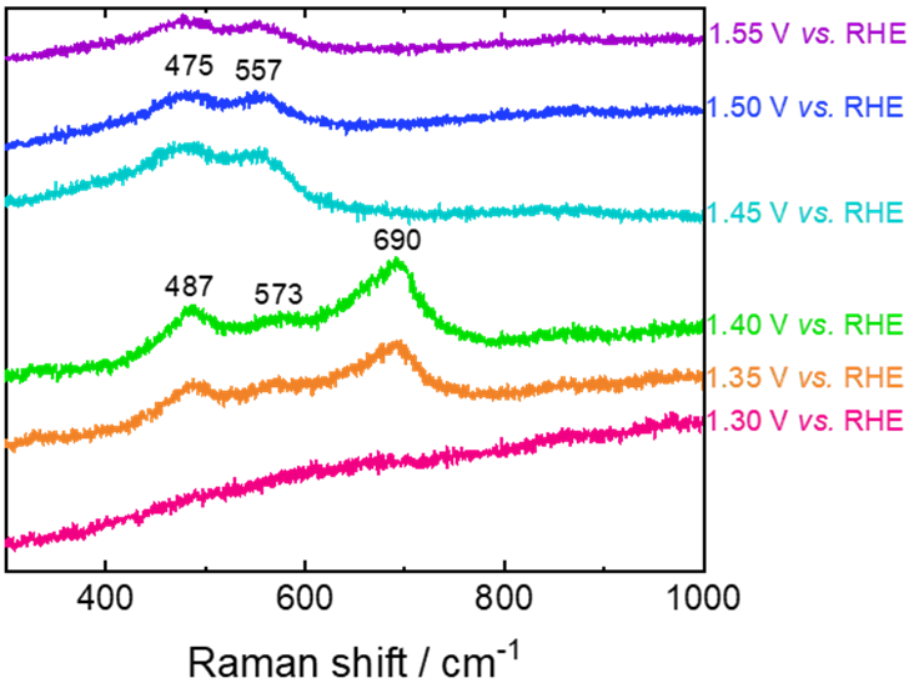

Figure 6. *In-situ* Raman spectra recorded on 25/25-NiFe@Mo_2CT_x catalyst at different electrode potentials. Before recording spectra, the catalyst was cycled 100 times between 0.15 and 1.50 V *vs.* RHE.

The 25/25-NiFe@Mo_2CT material is investigated by TEM-EELS electrode after 100 cycles at 50 mV s^{-1} between 0.2 and 1.55 V *vs.* RHE. The TEM image of the aged sample in Figure 7a display areas with bunches of nanoparticles (white arrows) deposited on the MXene support (black arrow). EF-SAED of the aged MXene support (Figure 7b) shows rings corresponding to the original hexagonal structure of Mo_2CT_x. The in-plane unit cell parameter deduced from the diffraction pattern is around 2.9 Å, in very good agreement with the XRD refinement of Deeva *et al.* [83]. Given the inhomogeneous contrast in Figure 7a and the diffraction pattern, one can conclude that the MXene sheets are disorganized although their crystallographic structure is maintained. The chemical analysis by EELS (Figure 7c) evidences the presence of molybdenum (Mo-$M_{4,5}$ edge), of carbon (C-K edge) and of potassium (K-$L_{2,3}$ edge). The presence of potassium assesses the fact that this region of the sample was in contact with the KOH electrolyte and has thus undergone the electrochemical processes. The oxygen K edge (Figure

7d) displays fine structures significantly different from those reported by Lajaunie et al. [85] for different molybdenum oxides (MoO_2 and MoO_3), suggesting that the MXene support has not been deeply oxidized. All this study shows the MXene support possesses a good chemical stability during electrochemical cycles.

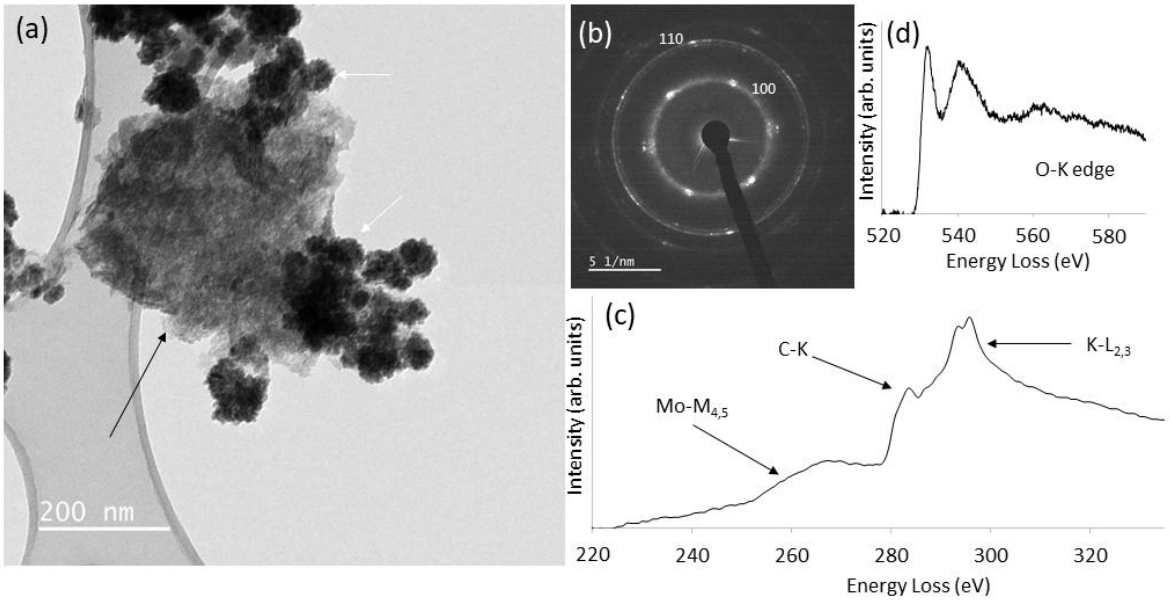

Figure 7. (a) TEM micrograph showing the support (black arrow) and the nanoparticles (white arrows), (b) EF SAED - pattern recorded on the MXene support, (c) EELS spectrum recorded on the MXene support around the C-K edge, (d) O-K edge recorded on the MXene support.

EF-SAED performed on the aged Ni_xFe_y particles (white arrows in Figure 7a) reveal identical patterns to those obtained before cycling (Figures S9b and S9c), as for EELS measurements concerning Fe-$L_{2,3}$ and Ni-$L_{2,3}$ edges (Figures S9d and S9e). These results confirm the reversibility of the oxyhydroxide layer formation previously evidenced by *in situ* Raman spectroscopy. At last, the O-K edge reveals the presence of oxygen in the nanoparticles with a fine structure presenting a difference in the relative intensities of the peaks A and B. All these findings are consistent with a modification of the surface of the nanoparticles inherent to the modification of their morphology.

CONCLUSION

A polyol-assisted solvothermal route is proposed to synthesize composite materials consisting of Ni_xFe_y active phases supported on Mo_2CT_x MXene. The synthesis procedure has little effect on the Mo_2CT_x MXene structure and composition. The anchoring sites of the MXene support favor the nucleation and growth of Ni_xFe_y nanoalloys leading to a very efficient active phase towards the OER in alkaline medium. Catalytic properties of Ni_xFe_y are directly related to the Ni/Fe ratio, the most efficient catalyst being obtained for a ratio of 2.66 (25/25-NiFe@Mo_2CT_x). This material exhibits an outstanding activity with an electrode potential of only 1.50 V *vs.* RHE for a current density of 10 mA cm^{-2} and a Tafel slope of only 34 mV dec^{-1}. This amazingly low Tafel slope value makes this material a serious candidate to drive current densities required in a real electrolysis cell at low overpotentials and places this catalyst among the best ever reported to date. Thanks to numerous characterization methods, it was highlighted that the high activity of the active phase is mainly due to a combination of 3 factors: the low size of alloyed Ni_xFe_y particles induced by the presence of the MXene in the synthesis reactor, the lower charge transfer resistance between the active phase and the MXene support due to protection of the interface by the Ni_xFe_y particles (active phase/support interaction) and the formation of the active β-Ni(Fe)OOH phase.

Long-term experiments have shown that this material also was stable for the OER. TEM-EELS analyses of aged material did not evidence any core oxidation of the MXene, even for potential beyond the irreversible peak potential value. This indicates that only surface Mo atoms are irreversibly oxidized. Under these conditions, MXene sheets are disorganized while keeping their crystallographic structure. Potential cycling experiments indicate a surface reversibility

603 (chemical reset) for Ni_xFe nanoalloys, the oxyhydroxide formed at OER potentials being totally
604 reduced during the negative going scan.
605 Considering the simplicity of the synthesis route and the possibility to tune easily chemical
606 composition of both MXene substrate and active phase, one can reasonably assume that this
607 study paves the way to the emergence of a new class of highly efficient MXene based composite
608 catalysts, thus contributing to the development of energy storage and conversion systems with
609 improved electrical performances.
610

611 **ACKNOWLEDGMENT**

612 The authors acknowledge financial support from the "Agence Nationale de la Recherche"
613 (reference ANR-18-CE08-014 – MXENECAT project). The authors acknowledge the European
614 Union (ERDF) and Région Nouvelle Aquitaine for the funding of MABATRI project (reference
615 2021-16148810). This work pertains to the French government program "Investissements
616 d'Avenir" (EUR INTREE, reference ANR-18-EURE-0010).
617

618 **REFERENCES**

619 [1] Anantharaj S, Ede S R, Sakthikumar K, Karthick K, Mishra S and Kundu S 2016 Recent
620 Trends and Perspectives in Electrochemical Water Splitting with an Emphasis on Sulfide,
621 Selenide, and Phosphide Catalysts of Fe, Co, and Ni: A Review *ACS Catal.* **6** 8069–97
622 [2] Nong H N, Reier T, Oh H-S, Gliech M, Paciok P, Vu T H T, Teschner D, Heggen M,
623 Petkov V, Schlögl R, Jones T and Strasser P 2018 A unique oxygen ligand environment
624 facilitates water oxidation in hole-doped IrNiOx core–shell electrocatalysts *Nat. Catal.* **1**
625 841–51
626 [3] Song J, Wei C, Huang Z-F, Liu C, Zeng L, Wang X and Xu Z J 2020 A review on

fundamentals for designing oxygen evolution electrocatalysts *Chem. Soc. Rev.* **49** 2196–214

[4] Zhang R, Wang L, Pan L, Chen Z, Jia W, Zhang X and Zou J-J 2020 Solid-acid-mediated electronic structure regulation of electrocatalysts and scaling relation breaking of oxygen evolution reaction *Appl. Catal. B Environ.* **277** 119237

[5] Habrioux A, Morais C, Napporn T W and Kokoh B 2020 Recent trends in hydrogen and oxygen electrocatalysis for anion exchange membrane technologies *Curr. Opin. Electrochem.* **21** 146–59

[6] Zhang L, Fan Q, Li K, Zhang S and Ma X 2020 First-row transition metal oxide oxygen evolution electrocatalysts: regulation strategies and mechanistic understandings *Sustain. Energy Fuels* **4** 5417–32

[7] Cai Z, Bu X, Wang P, Ho J C, Yang J and Wang X 2019 Recent advances in layered double hydroxide electrocatalysts for the oxygen evolution reaction *J. Mater. Chem. A* **7** 5069–89

[8] Kang J, Qiu X, Hu Q, Zhong J, Gao X, Huang R, Wan C, Liu L-M, Duan X and Guo L 2021 Valence oscillation and dynamic active sites in monolayer NiCo hydroxides for water oxidation *Nat. Catal.* **4** 1050–8

[9] Li W, Xiong D, Gao X and Liu L 2019 The oxygen evolution reaction enabled by transition metal phosphide and chalcogenide pre-catalysts with dynamic changes *Chem. Commun.* **55** 8744–63

[10] Xu J, Li J, Xiong D, Zhang B, Liu Y, Wu K-H, Amorim I, Li W and Liu L 2018 Trends in activity for the oxygen evolution reaction on transition metal (M = Fe, Co, Ni) phosphide pre-catalysts *Chem. Sci.* **9** 3470–6

650 [11] Tareen A K, Priyanga G S, Khan K, Pervaiz E, Thomas T and Yang M 2019 Nickel-
651 Based Transition Metal Nitride Electrocatalysts for the Oxygen Evolution Reaction
652 *ChemSusChem* **12** 3941–54
653 [12] Peng L, Wang C, Wang Q, Shi R, Zhang T and Waterhouse G I N 2021 Rationally
654 Designed Ni–Ni 3 S 2 Interfaces for Efficient Overall Water Electrolysis *Adv. Energy*
655 *Sustain. Res.* **2** 2100078
656 [13] Masa J, Sinev I, Mistry H, Ventosa E, Mata M de la, Arbiol J, Muhler M, Cuenya B R
657 and Schuhmann W 2017 Ultrathin High Surface Area Nickel Boride (NixB) Nanosheets
658 as Highly Efficient Electrocatalyst for Oxygen Evolution *Adv. Energy Mater.* **7** 1700381
659 [14] Song F, Busch M M, Lassalle-Kaiser B, Hsu C-S, Petkucheva E, Bensimon M, Chen H
660 M, Corminboeuf C and Hu X 2019 An Unconventional Iron Nickel Catalyst for the
661 Oxygen Evolution Reaction *ACS Cent. Sci.* **5** 558–68
662 [15] Zhang G, Zeng J, Yin J, Zuo C, Wen P, Chen H and Qiu Y 2021 Iron-facilitated surface
663 reconstruction to in-situ generate nickel–iron oxyhydroxide on self-supported FeNi alloy
664 fiber paper for efficient oxygen evolution reaction *Appl. Catal. B Environ.* **286** 119902
665 [16] Suen N-T, Hung S-F, Quan Q, Zhang N, Xu Y-J and Chen H M 2017 Electrocatalysis for
666 the oxygen evolution reaction: recent development and future perspectives *Chem. Soc.*
667 *Rev.* **46** 337–65
668 [17] Gong M and Dai H 2015 A mini review of NiFe-based materials as highly active oxygen
669 evolution reaction electrocatalysts *Nano Res.* **8** 23–39
670 [18] Song F and Hu X 2014 Exfoliation of layered double hydroxides for enhanced oxygen
671 evolution catalysis *Nat. Commun.* **5** 4477
672 [19] Trotochaud L, Young S L, Ranney J K and Boettcher S W 2014 Nickel-Iron

673 oxyhydroxide oxygen-evolution electrocatalysts: The role of intentional and incidental
674 iron incorporation *J. Am. Chem. Soc.* **136** 6744–53
675 [20] Xiao H, Shin H and Goddard W A 2018 Synergy between Fe and Ni in the optimal
676 performance of (Ni,Fe)OOH catalysts for the oxygen evolution reaction *Proc. Natl. Acad.*
677 *Sci.* **115** 5872–7
678 [21] Bao F, Kemppainen E, Dorbandt I, Xi F, Bors R, Maticiuc N, Wenisch R, Bagacki R,
679 Schary C, Michalczik U, Bogdanoff P, Lauermann I, van de Krol R, Schlatmann R and
680 Calnan S 2021 Host, Suppressor, and Promoter—The Roles of Ni and Fe on Oxygen
681 Evolution Reaction Activity and Stability of NiFe Alloy Thin Films in Alkaline Media
682 *ACS Catal.* **11** 10537–52
683 [22] Lee S, Banjac K, Lingenfelder M and Hu X 2019 Oxygen Isotope Labeling Experiments
684 Reveal Different Reaction Sites for the Oxygen Evolution Reaction on Nickel and Nickel
685 Iron Oxides *Angew. Chemie* **131** 10401–5
686 [23] Spanos I, Masa J, Zeradjanin A and Schlögl R 2021 The Effect of Iron Impurities on
687 Transition Metal Catalysts for the Oxygen Evolution Reaction in Alkaline Environment:
688 Activity Mediators or Active Sites? *Catal. Letters* **151** 1843–56
689 [24] Feng Y, Yu X-Y and Paik U 2016 N-doped graphene layers encapsulated NiFe alloy
690 nanoparticles derived from MOFs with superior electrochemical performance for oxygen
691 evolution reaction *Sci. Rep.* **6** 34004
692 [25] Liu S, Cao E, Chen Z, Wu H, Liu B, Yang J, Du S and Ren Z 2021 Promoting
693 Electrocatalytic Oxygen Evolution of Ultrasmall NiFe (Hydr)oxide Nanoparticles by
694 Graphene-Support Effects *ChemSusChem* **14** 5508–16
695 [26] Li Y, Zou Q, Li Z, Xie D, Niu Y, Zou J, Zeng X and Huang J 2022 MOF derived Ni-Fe

based alloy carbon materials for efficient bifunctional electrocatalysts applied in Zn-air battery *Appl. Surf. Sci.* **572** 151286

[27] Ma W, Ma R, Wang C, Liang J, Liu X, Zhou K and Sasaki T 2015 A Superlattice of Alternately Stacked Ni–Fe Hydroxide Nanosheets and Graphene for Efficient Splitting of Water *ACS Nano* **9** 1977–84

[28] Wang H-F, Tang C and Zhang Q 2015 Towards superior oxygen evolution through graphene barriers between metal substrates and hydroxide catalysts *J. Mater. Chem. A* **3** 16183–9

[29] Shi M, Sun X, Bai Q, Zhang Y, Yu S, Liu M, Wang L, Yu W W and Sui N 2022 Graphdiyne/graphene heterostructure supported NiFe layered double hydroxides for oxygen evolution reaction *Colloids Surfaces A Physicochem. Eng. Asp.* **637** 128217

[30] Gong Z, Liu R, Gong H, Ye G, Liu J J, Dong J, Liao J, Yan M, Liu J J, Huang K, Xing L, Liang J, He Y and Fei H 2021 Constructing a Graphene-Encapsulated Amorphous/Crystalline Heterophase NiFe Alloy by Microwave Thermal Shock for Boosting the Oxygen Evolution Reaction *ACS Catal.* **11** 12284–92

[31] Filimonenkov I S, Bouillet C, Kéranguéven G, Simonov P A, Tsirlina G A and Savinova E R 2019 Carbon materials as additives to the OER catalysts: RRDE study of carbon corrosion at high anodic potentials *Electrochim. Acta* **321** 134657

[32] Wang Y, Wu Q, Zhang B, Tian L, Li K and Zhang X 2020 Recent Advances in Transition Metal Carbide Electrocatalysts for Oxygen Evolution Reaction *Catalysts* **10** 1164

[33] Liu H J and Dong B 2021 Recent advances and prospects of MXene-based materials for electrocatalysis and energy storage *Mater. Today Phys.* **20** 100469

[34] Qiao J, Kong L, Xu S, Lin K, He W, Ni M, Ruan Q, Zhang P, Liu Y, Zhang W, Pan L and Sun Z M 2021 Research progress of MXene-based catalysts for electrochemical water-splitting and metal-air batteries *Energy Storage Mater.* **43** 509–30

[35] Browne M P, Tyndall D and Nicolosi V 2022 The potential of MXene materials as a component in the catalyst layer for the Oxygen Evolution Reaction *Curr. Opin. Electrochem.* **34** 101021

[36] Lim K R G, Shekhirev M, Wyatt B C, Anasori B, Gogotsi Y and Seh Z W 2022 Fundamentals of MXene synthesis *Nat. Synth. 2022 18* **1** 601–14

[37] Rahman U U, Humayun M, Ghani U, Usman M, Ullah H, Khan A, El-Metwaly N M and Khan A 2022 MXenes as Emerging Materials: Synthesis, Properties, and Applications *Mol. 2022, Vol. 27, Page 4909* **27** 4909

[38] Nashim A and Parida K 2022 A Glimpse on the plethora of applications of prodigious material MXene *Sustain. Mater. Technol.* **32** e00439

[39] Naguib M, Barsoum M W and Gogotsi Y 2021 Ten Years of Progress in the Synthesis and Development of MXenes *Adv. Mater.* **33** 1–10

[40] Mohammadi A V, Rosen J and Gogotsi Y 2021 The world of two-dimensional carbides and nitrides (MXenes) *Science (80-.).* **372**

[41] Benchakar M, Bilyk T, Garnero C, Loupias L, Morais C, Pacaud J, Canaff C, Chartier P, Morisset S, Guignard N, Mauchamp V, Célérier S and Habrioux A 2019 MXene Supported Cobalt Layered Double Hydroxide Nanocrystals: Facile Synthesis Route for a Synergistic Oxygen Evolution Reaction Electrocatalyst *Adv. Mater. Interfaces* **6** 1–11

[42] Nayak P, Yang M, Wang Z, Li X, Miao R and Compton R G 2022 Single-entity Ti3C2Tx MXene electro-oxidation *Appl. Mater. Today* **26** 101335

[43] Lorencova L, Bertok T, Dosekova E, Holazova A, Paprckova D, Vikartovska A, Sasinkova V, Filip J, Kasak P, Jerigova M, Velic D, Mahmoud K A and Tkac J 2017 Electrochemical performance of Ti3C2Tx MXene in aqueous media: towards ultrasensitive H2O2 sensing *Electrochim. Acta* **235** 471–9

[44] Chen J, Long Q, Xiao K, Ouyang T, Li N, Ye S and Liu Z-Q Q 2021 Vertically-interlaced NiFeP/MXene electrocatalyst with tunable electronic structure for high-efficiency oxygen evolution reaction *Sci. Bull.* **66** 1063–72

[45] Shinde P V., Mane P, Chakraborty B and Sekhar Rout C 2021 Spinel NiFe2O4 nanoparticles decorated 2D Ti3C2 MXene sheets for efficient water splitting: Experiments and theories *J. Colloid Interface Sci.* **602** 232–41

[46] Yu M, Zhou S, Wang Z, Zhao J and Qiu J 2018 Boosting electrocatalytic oxygen evolution by synergistically coupling layered double hydroxide with MXene *Nano Energy* **44** 181–90

[47] Wang Y, Zhou Y, Han M, Xi Y, You H, Hao X, Li Z, Zhou J, Song D, Wang D and Gao F 2019 Environmentally-Friendly Exfoliate and Active Site Self-Assembly: Thin 2D/2D Heterostructure Amorphous Nickel–Iron Alloy on 2D Materials for Efficient Oxygen Evolution Reaction *Small* **15** 1–8

[48] Li Z, Wang X, Ren J and Wang H 2022 NiFe LDH/Ti3C2Tx/nickel foam as a binder-free electrode with enhanced oxygen evolution reaction performance *Int. J. Hydrogen Energy* **47** 3886–92

[49] Wang J, He P, Shen Y, Dai L, Li Z, Wu Y and An C 2021 FeNi nanoparticles on Mo2TiC2Tx MXene@nickel foam as robust electrocatalysts for overall water splitting *Nano Res.* **14** 3474–81

[50] Chen Y, Yao H, Kong F, Tian H, Meng G, Wang S, Mao X, Cui X, Hou X and Shi J 2021 V2C MXene synergistically coupling FeNi LDH nanosheets for boosting oxygen evolution reaction *Appl. Catal. B Environ.* **297** 120474

[51] Benchakar M, Natu V, Elmelegy T A, Sokol M, Snyder J, Comminges C, Morais C, Célérier S, Habrioux A and Barsoum M W 2020 On a Two-Dimensional MoS2/Mo2CTx Hydrogen Evolution Catalyst Obtained by the Topotactic Sulfurization of Mo2CTx MXene *J. Electrochem. Soc.* **167** 124507

[52] Larcher D and Patrice R 2000 Preparation of metallic powders and alloys in polyol media: A thermodynamic approach *J. Solid State Chem.* **154** 405–11

[53] Fievet F, Lagier J P, Blin B, Beaudoin B and Figlarz M 1989 Homogeneous and heterogeneous nucleations in the polyol process for the preparation of micron and submicron size metal particles *Solid State Ionics* **32–33** 198–205

[54] Tang F, Liu T, Jiang W and Gan L 2020 Windowless thin layer electrochemical Raman spectroscopy of Ni-Fe oxide electrocatalysts during oxygen evolution reaction *J. Electroanal. Chem.* **871** 114282

[55] Célérier S, Hurand S, Garnero C, Morisset S, Benchakar M, Habrioux A, Chartier P, Mauchamp V, Findling N, Lanson B and Ferrage E 2019 Hydration of Ti 3 C 2 T x MXene: An Interstratification Process with Major Implications on Physical Properties *Chem. Mater.* **31** 454–61

[56] Liu J, Chen T, Juan P, Peng W, Li Y, Zhang F and Fan X 2018 Hierarchical Cobalt Borate/MXenes Hybrid with Extraordinary Electrocatalytic Performance in Oxygen Evolution Reaction *ChemSusChem* **11** 3758–65

[57] Yu M, Wang Z, Liu J, Sun F, Yang P and Qiu J 2019 A hierarchically porous and

788 hydrophilic 3D nickel–iron/MXene electrode for accelerating oxygen and hydrogen
789 evolution at high current densities *Nano Energy* **63** 103880
790 [58] Cortez O A, Moura F J, de Albuquerque Brocchi E, de Siqueira R N C and de Souza R F
791 M 2014 Fe-Ni Alloy Synthesis Based on Nitrates Thermal Decomposition Followed by
792 H2 Reduction *Metall. Mater. Trans. B* **45** 2033–9
793 [59] Patterson A L 1939 The Scherrer Formula for X-Ray Particle Size Determination *Phys.*
794 *Rev.* **56** 978–82
795 [60] Halim J, Kota S, Lukatskaya M R, Naguib M, Zhao M-Q, Moon E J, Pitock J, Nanda J,
796 May S J, Gogotsi Y and Barsoum M W 2016 Synthesis and Characterization of 2D
797 Molybdenum Carbide (MXene) *Adv. Funct. Mater.* **26** 3118–27
798 [61] Hu C, Lai C-C, Tao Q, Lu J, Halim J, Sun L, Zhang J, Yang J, Anasori B, Wang J, Sakka
799 Y, Hultman L, Eklund P, Rosen J and Barsoum M W 2015 Mo2Ga2C: a new ternary
800 nanolaminated carbide *Chem. Commun.* **51** 6560–3
801 [62] Kuznetsov D A, Chen Z, Kumar P V, Tsoukalou A, Kierzkowska A, Abdala P M,
802 Safonova O V, Fedorov A and Müller C R 2019 Single Site Cobalt Substitution in 2D
803 Molybdenum Carbide (MXene) Enhances Catalytic Activity in the Hydrogen Evolution
804 Reaction *J. Am. Chem. Soc.* **141** 17809–16
805 [63] Benchakar M, Loupias L, Garnero C, Bilyk T, Morais C, Canaff C, Guignard N, Morisset
806 S, Pazniak H, Hurand S, Chartier P, Pacaud J, Mauchamp V, Barsoum M W, Habrioux A
807 and Célérier S 2020 One MAX phase, different MXenes: A guideline to understand the
808 crucial role of etching conditions on Ti3C2Tx surface chemistry *Appl. Surf. Sci.* **530**
809 [64] Bayle-Guillemaud P, Barbier A and Mocuta C 2001 Development of a quantitative
810 energy filtering TEM method to study a reactive NiO/80Ni20Fe interface

811 *Ultramicroscopy* **88** 99–110

812 [65] Nelson A T, White J T, Andersson D A, Aguiar J A, McClellan K J, Byler D D, Short M
813 P and Stanek C R 2014 Thermal Expansion, Heat Capacity, and Thermal Conductivity of
814 Nickel Ferrite (NiFe 2 O 4) ed M White *J. Am. Ceram. Soc.* **97** 1559–65

815 [66] Rasheed P A, Pandey R P, Jabbar K A, Ponraj J and Mahmoud K A 2019 Sensitive
816 electrochemical detection of l-cysteine based on a highly stable Pd@Ti3C2T:X(MXene)
817 nanocomposite modified glassy carbon electrode *Anal. Methods* **11** 3851–6

818 [67] Lorencova L, Bertok T, Filip J, Jerigova M, Velic D, Kasak P, Mahmoud K A and Tkac J
819 2018 Highly stable Ti3C2Tx (MXene)/Pt nanoparticles-modified glassy carbon electrode
820 for H2O2 and small molecules sensing applications *Sensors Actuators B Chem.* **263** 360–8

821 [68] Qiu Y, Xin L and Li W 2014 Electrocatalytic Oxygen Evolution over Supported Small
822 Amorphous Ni–Fe Nanoparticles in Alkaline Electrolyte *Langmuir* **30** 7893–901

823 [69] Kostecki R and McLarnon F 1997 Electrochemical and In Situ Raman Spectroscopic
824 Characterization of Nickel Hydroxide Electrodes: I. Pure Nickel Hydroxide *J.*
825 *Electrochem. Soc.* **144** 485–93

826 [70] Lyons M E G and Brandon M P 2008 The oxygen evolution reaction on passive oxide
827 covered transition metal electrodes in alkaline solution part ii - cobalt *Int. J. Electrochem.*
828 *Sci.* **3** 1425–62

829 [71] Machado S A S and Avaca L A 1994 The hydrogen evolution reaction on nickel surfaces
830 stabilized by H-absorption *Electrochim. Acta* **39** 1385–91

831 [72] Yan W, Wang D and Botte G G 2012 Electrochemical decomposition of urea with Ni-
832 based catalysts *Appl. Catal. B Environ.* **127** 221–6

833 [73] Brown I J and Sotiropoulos S 2000 Preparation and characterization of microporous Ni

coatings as hydrogen evolving cathodes *J. Appl. Electrochem.* **30** 107–11

[74] Armstrong R D and Henderson M 1972 Impedance plane display of a reaction with an adsorbed intermediate *J. Electroanal. Chem. Interfacial Electrochem.* **39** 81–90

[75] Ruhl J, Riegger L M, Ghidiu M and Zeier W G 2021 Impact of Solvent Treatment of the Superionic Argyrodite Li6PS5Cl on Solid-State Battery Performance *Adv. Energy Sustain. Res.* **2** 2000077

[76] Doyle R L and Lyons M E G 2013 An electrochemical impedance study of the oxygen evolution reaction at hydrous iron oxide in base *Phys. Chem. Chem. Phys.* **15** 5224–37

[77] Yu M, Budiyanto E and Tüysüz H 2022 Principles of Water Electrolysis and Recent Progress in Cobalt-, Nickel-, and Iron-Based Oxides for the Oxygen Evolution Reaction *Angew. Chemie - Int. Ed.* **61**

[78] Görlin M, Chernev P, Ferreira de Araújo J, Reier T, Dresp S, Paul B, Krähnert R, Dau H and Strasser P 2016 Oxygen Evolution Reaction Dynamics, Faradaic Charge Efficiency, and the Active Metal Redox States of Ni-Fe Oxide Water Splitting Electrocatalysts *J. Am. Chem. Soc.* **138** 5603–14

[79] Louie M W and Bell A T 2013 An investigation of thin-film Ni-Fe oxide catalysts for the electrochemical evolution of oxygen *J. Am. Chem. Soc.* **135** 12329–37

[80] Lee S, Bai L and Hu X 2020 Deciphering Iron-Dependent Activity in Oxygen Evolution Catalyzed by Nickel-Iron Layered Double Hydroxide *Angew. Chem. Int. Ed. Engl.* **59** 8072–7

[81] Marshall A T and Vaisson-Béthune L 2015 Avoid the quasi-equilibrium assumption when evaluating the electrocatalytic oxygen evolution reaction mechanism by Tafel slope analysis *Electrochem. commun.* **61** 23–6

[82] Yeo B S and Bell A T 2012 In Situ Raman Study of Nickel Oxide and Gold-Supported Nickel Oxide Catalysts for the Electrochemical Evolution of Oxygen *J. Phys. Chem. C* **116** 8394–400

[83] Deeva E B, Kurlov A, Abdala P M, Lebedev D, Kim S M, Gordon C P, Tsoukalou A, Fedorov A and Müller C R 2019 In Situ XANES/XRD Study of the Structural Stability of Two-Dimensional Molybdenum Carbide Mo2CT x: Implications for the Catalytic Activity in the Water-Gas Shift Reaction *Chem. Mater.* **31** 4505–13

[84] Lajaunie L, Boucher F, Dessapt R and Moreau P 2015 Quantitative use of electron energy-loss spectroscopy Mo-M2,3 edges for the study of molybdenum oxides *Ultramicroscopy* **149** 1–8